International Journal of Advanced Engineering and Technology Research
ISSN: 3106-8677 (Print), ISSN: 3106-8685 (Online) | Vol. 1, No. 2, 2026

Broadband Low-Frequency Sound Absorption Based on Helmholtz Resonators Embedded with Microperforated Panel

Bo Huang

School of Physics and Optoelectronic Engineering, Guangdong University of Technology, Guangzhou 510006, China

Abstract: This study proposes a novel Helmholtz resonator embedded with a microperforated panel (HREMPP) for broadband low-frequency sound absorption. A theoretical model was validated by simulations. The 50-mm-thick HREMPP unit achieves near-perfect absorption at 250 Hz with a bandwidth 50% wider than a conventional Helmholtz resonator. Parameter analysis reveals how neck radius, neck length, and micro-perforation radius tune the performance. By parallel coupling two units with different neck radii (2 mm and 3 mm) while maintaining a 50 mm total thickness, a broadband metamaterial is created. It exhibits two absorption peaks at 208 Hz and 284 Hz, forming a continuous broad absorption band from 176 Hz to 358 Hz. This work provides a design for ultra-thin, broadband, low-frequency acoustic absorbers.

Keywords: Helmholtz resonator, sound absorption, noise control, low-frequency.

1. Introduction

With the continuous advancement of modernization, noise pollution has become increasingly prominent. Taking low-frequency noise pollution as an example, porous materials exhibit significantly limited sound absorption performance in the low-frequency range, often requiring structural thickness to be increased to a scale comparable to the wavelength. Although Helmholtz resonators (HR) and microperforated panels (MPP) can control low-frequency noise, they still have notable limitations. The resonance mechanism of Helmholtz resonators results in a relatively narrow effective absorption bandwidth, while microperforated panels require a corresponding increase in thickness. This remains a significant challenge for practical applications.

The emergence of acoustic metamaterials has provided new solutions to this issue. For instance, membrane-type acoustic metamaterials, Fabry-Pérot(FP) resonators [1-3] and Helmholtz resonator-based metamaterials [4-6] have been employed to design (deep) subwavelength-thickness sound absorbers, demonstrating high absorption performance for low-frequency noise. Zhang et al. [7] combined bent channels with embedded holes and established a theoretical model for the unit structure's sound absorption based on thermo-viscous theory and the transfer matrix method, achieving perfect absorption of low-frequency noise. Huang et al. [4] designed a Helmholtz resonator (HR) with embedded necks, enhancing the impedance modulation capability of the overall structure and realizing perfect sound absorption at low frequencies with a thickness of only $1/50\lambda$ (where λ represents the wavelength). Duan et al. [8] introduced a rubber coating and embedded metal necks on the inner surface of a metal hexagonal honeycomb HR, achieving perfect underwater low-frequency sound absorption at subwavelength dimensions ($\lambda/300$). However, these sound-absorbing structures exhibit excellent performance only near a single frequency.

To achieve broadband low-frequency sound absorption, a straightforward approach is to arrange multiple unit structures in parallel to increase the number of absorption peaks. Zhang and Hu [9] combined six folded labyrinthine channel structures in parallel, achieving efficient sound absorption within the 105 Hz–175 Hz range, with an overall thickness of 18 cm. Yang et al. [10] designed a sound absorber composed of 16 folded FP resonance structures, enabling ultra-broadband high absorption in the 400 Hz–3000 Hz range, with a thickness exceeding 10 cm. Another method involves using optimization algorithms or machine learning to design broadband sound-absorbing structural parameters. Zhen et al. [11] employed deep learning techniques to significantly accelerate the inverse design process, achieving quasi-perfect sound absorption (absorption coefficient $\alpha \geq 0.9$) within the 350–530 Hz band using only nine resonators.

Based on previous research, this study proposes a Helmholtz resonator structure with an embedded micro-perforated panel (HR embedded with MPP, HREMPP) and designs a low-frequency broadband sound-absorbing metamaterial. A theoretical model of sound absorption and a finite element numerical model were established. The complex frequency plane method was used to analyze the mechanism by which the unit's low-frequency sound absorption performance can be tuned without altering the overall thickness. Two units of equal thickness were coupled in parallel to form a broadband sound-absorbing metamaterial with dimensions comparable to the wavelength.

2. Electroacoustic Analogy Theoretical Model

The proposed sound-absorbing metamaterial consists of two HREMPPs connected in parallel. As shown in Figure1(a), each HREMPP is divided into four parts: the neck, the micro-perforated panel, the side cavity, and the back cavity. Figure1(b) illustrates the geometry and dimensions of each component. The embedded neck is arranged parallel to the micro-perforated panel, with a neck radius of r_n and length l_n. The micro-perforated panel contains np micro-perforations, each with a radius r_p, a panel thickness t_{fp}, a periodic spacing dp, and an inner wall thickness t. The unit has a height H, with a square base of side length a.

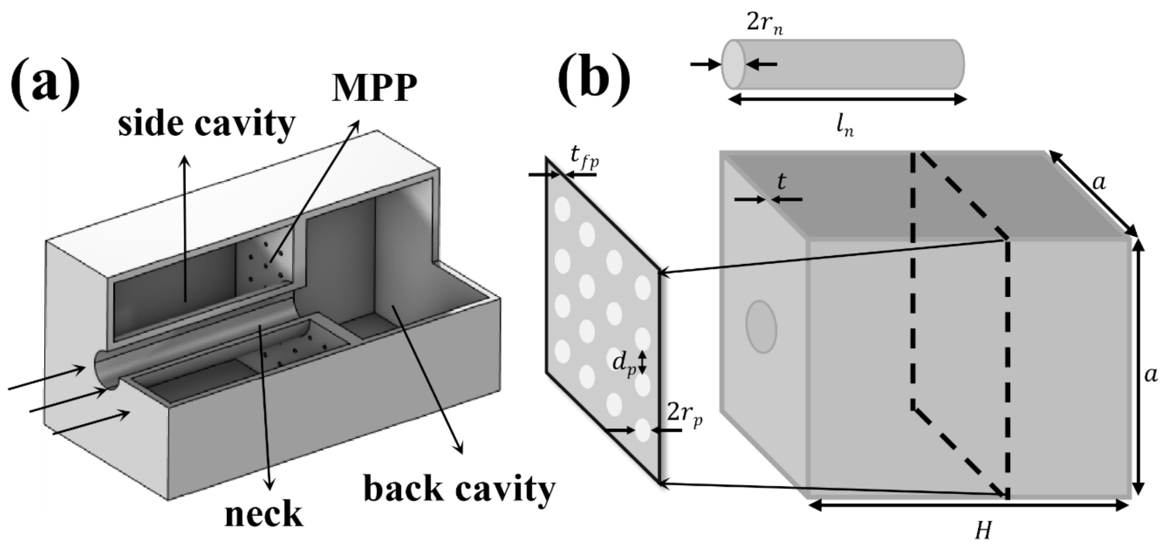

Figure 1. HREMPP model (a) 3D model diagram; (b) Structural parameters

The impedance connections between the various parts are shown in Figure 2(a). Using the electro-acoustic analogy method, the surface acoustic impedance Z_{sp} of the HREMPP structure is derived, where P_0 and Z_0 represent the incident sound pressure and the acoustic impedance of air, respectively. Z_{n1} is the equivalent inductance M_1 and resistance R_1 of the neck, Z_{c1} is the equivalent capacitance of the back cavity; Z_{n2} is the equivalent inductance M_2 and resistance R_2 of the micro-perforated panel, and Z_{c2} is the equivalent capacitance of the side cavity. Therefore, Z_{sp} is expressed as

$$Z_{sp} = Z_{n1} + Z_{c1} + Z_{n2} + Z_{c2} \tag{1}$$

The impedance Z_{n1} of the neck hole can be calculated using Euler's equation as

$$Z_{n1} = \frac{j\omega\rho_0 t}{\sigma_1}\left[1 - \frac{2B_1(\chi_1\sqrt{-j})}{(\chi_1\sqrt{-j})B_0(\chi_1\sqrt{-j})}\right]^{-1} + \frac{\sqrt{2}\mu\chi_1}{2\sigma_1 r_n} + \frac{j\omega\rho_0\Delta t}{\sigma_1} \tag{2}$$

Where $\sigma_1 = \pi r_n^2/[(a-2t)^2 - n_p\pi r_p^2]$ is the perforation ratio of the neck relative to the cavity cross-section, and B_0 and B_1 are the first-kind zero-order Bessel function and first-order Bessel function, respectively. $\chi_1 = r_n\sqrt{\omega\rho_0/\mu}$ is the constant piercing of the neck. $\mu = 1.8\times10^{-5}\,\mathrm{Pa\cdot s}$ is the dynamic viscosity of air. $\Delta t = \Delta t_1 + \Delta t_2$ is terminal impedance correction value for the neck. Δt_1 is caused by the pressure discontinuity when radiating from the neck to the cavity. Δt_2 is caused by the pressure discontinuity radiating outward from the neck. Δt_1 and Δt_2 are respectively represented as

$$\Delta t_1 = 0.82[1 - 1.35\sigma_n + 0.31\sigma_n^3]r_n \tag{3}$$

$$\Delta t_2 = 0.82[1 - 0.235\sigma_n - 1.32\sigma_n^2 + 1.54\sigma_n^3 - 0.86\sigma_n^4]r_n \tag{4}$$

Where $\sigma_n^2 = \pi r_n^2/(a-2t)^2$ is the ratio of the neck area to the cross-sectional area of the cavity. The acoustic impedance of the back cavity can be expressed as

$$Z_{c1} = -jZ_0\cot[k_0(H - t - l_n)] \tag{5}$$

k_0 is the wavenumber in the air. The impedance of the microperforated panel Z_{n1} can be expressed as

$$Z_{n2} = \frac{8\mu t_{fp}}{\sigma_p r_p^2}\left[\left(1 + \frac{\chi_2^2}{32}\right)^{1/2} + \frac{\sqrt{2}r_p\chi_2}{16\,t_{fp}}\right] + \frac{j\omega t_{fp}}{\sigma_p}\left[1 + \left(9 + \frac{\chi_2^2}{2}\right)^{-1/2} + \frac{1.7r_p}{t_{fp}}\right] \tag{6}$$

Where $\chi_2 = r_p\sqrt{\omega\rho_0/\mu}$ is the perforation constant for a single micro perforation, and $\sigma_p = n_p\pi r_p^2/[(a-2t)^2 - \pi(r_n+t)^2]$ is the perforation ratio of the microperforated panel. The acoustic impedance of the side cavity can be expressed as

$$Z_{c2} = -jZ_0\cot\left[k_0\left(l_n - t - t_{fp}\right)\right] \tag{7}$$

The relative surface acoustic impedance of the HREMPP structure can be expressed as

$$z_{sp} = Z_{sp}/Z_0 = x_{sp} + jy_{sp} \tag{8}$$

Here, x_{sp} and y_{sp} are the relative specific resistance and relative specific reactance of HREMPP, respectively. Therefore, the sound absorption coefficient of HREMPP can be expressed as

$$\alpha_{sp} = \frac{4x_{sp}}{(1+x_{sp})^2 + y_{sp}^2} \tag{9}$$

When the perforated panel is absent, $Z_{n2} = 0$, the equivalent circuit of the HREMPP structure reduces to that of the HR structure. Therefore, the surface acoustic impedance Z_{hr}, relative surface acoustic impedance z_{hr}, and sound absorption coefficient of the HR structure can be expressed as follows:

$$Z_{hr} = Z_{n1} + Z_{c1} + Z_{c2} \tag{10}$$

$$z_{hr} = Z_{hr}/Z_0 = x_{hr} + jy_{hr} \tag{11}$$

$$\alpha_{sp} = \frac{4x_{hr}}{(1+x_{hr})^2 + y_{hr}^2} \tag{12}$$

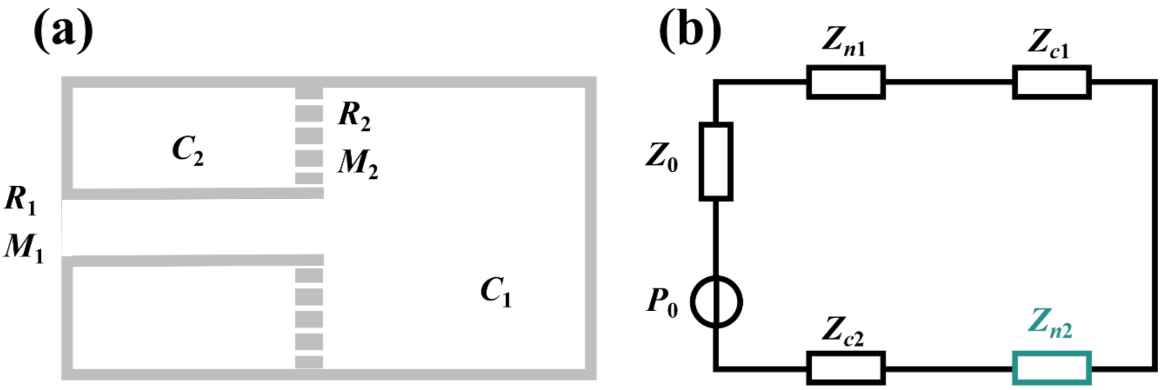

Figure 2. HREMPP model (a) Schematic diagram of acoustic impedance in each region; (b) Electroacoustic analog circuit

3. Analysis of Unit Sound Absorption Performance

3.1. Sound Absorption Mechanism

Figure 3(a) compares the sound absorption performance of the Helmholtz resonator with embedded micro-perforated panel (HREMPP) and the Helmholtz resonator (HR) both theoretically and numerically. The designed HREMPP unit has a height H=50 mm, a square base side length a=25 mm, a wall thickness t=1 mm, an embedded neck radius r_n=2.5 mm, an embedded neck length l_n=30 mm, the number of micro-perforations n_p=30, a perforation radius r_p=0.25 mm, a micro-perforated panel thickness t_{fp}=2 mm, and a periodic spacing d_p=3 mm. The theoretical and numerical results show good agreement, validating both models. The 50 mm-thick HREMPP achieves quasi-perfect absorption at 250 Hz, with a structural thickness less than 1/27 of the acoustic wavelength in air, and exhibits a half-absorption bandwidth of 90 Hz, ranging from 210 Hz to 300 Hz, demonstrating excellent low-frequency sound absorption performance at subwavelength scales. In contrast, the HR has a half-absorption bandwidth of only 36 Hz, ranging from 240 Hz to 276 Hz. Compared to the HR, the HREMPP demonstrates superior sound absorption capabilities in the frequency range of 100 Hz to 400 Hz. After introducing the micro-perforated panel into the cavity, the HR's sound absorption coefficient at the peak frequency increased by 54.28%, and its half-absorption bandwidth expanded by 50.00%. As shown in Figure 3(c), the sound pressure distribution in the HREMPP is similar with that in the HR, indicating that Helmholtz resonance can also be triggered in the HREMPP. Under resonance conditions, high sound pressure accumulates throughout the HREMPP cavity, meaning both the side and back cavity sections participate in sound propagation, jointly enhancing the broadband and tunable absorption performance of the HREMPP. As illustrated in Figure 3(d), the instantaneous sound velocity inside the HREMPP neck and micro-perforations increases, exceeding the velocity amplitude inside the cavity. The acoustic energy within the perforations is dissipated and converted into other forms of energy, thereby achieving near-perfect sound absorption at the target frequency.

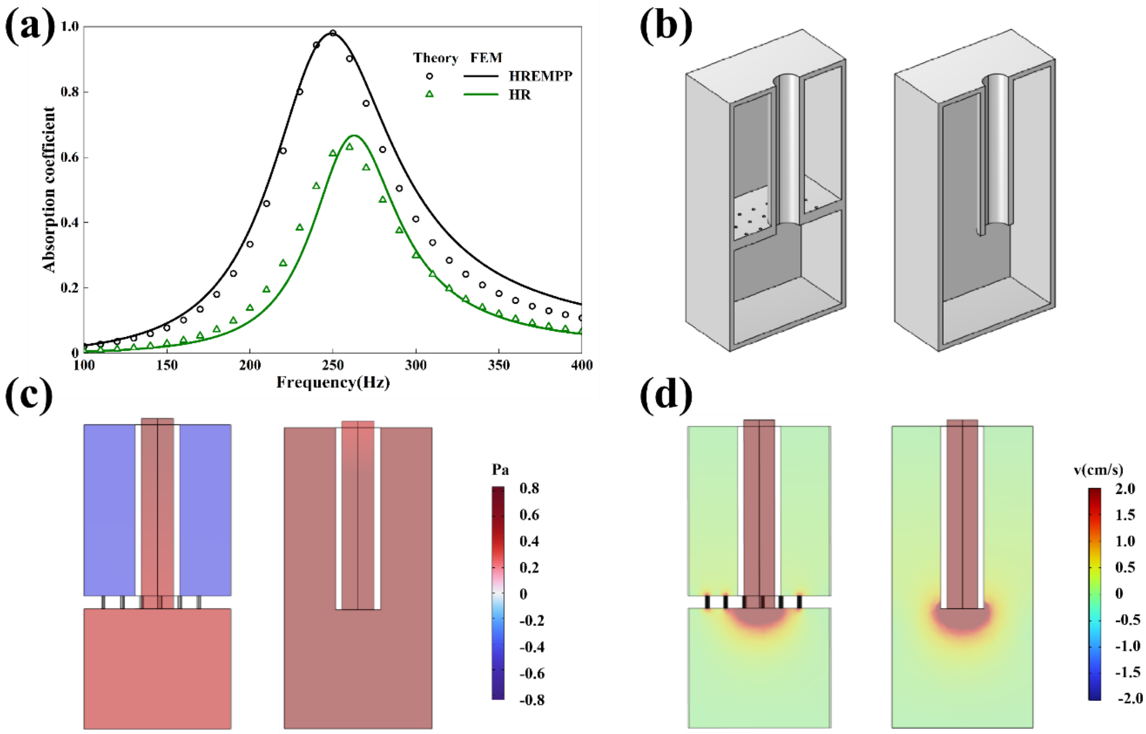

Figure 3. Comparison of sound absorption performance between HR and HREMPP (a) sound absorption coefficient comparison chart; (b) 3D model; (c) Sound pressure comparison diagram at resonance frequency; (d) Comparison of sound velocity at resonance frequency

3.2. The Effect of Neck Radius on Sound Absorption Performance

This section investigates the effect of varying the neck radius on the sound absorption performance of the unit. Only the neck radius is altered, while other parameters of the unit remain unchanged. Figure 4(a) shows the sound absorption coefficients for different neck radius, where the theoretical solutions and numerical solutions are represented by solid lines and hollow circles, respectively. It can be observed that the trends of the theoretical and numerical solutions are highly consistent. As the neck radius increases from 2.0 mm to 3.0 mm, the resonant absorption peak shifts toward higher frequencies, the peak absorption value gradually decreases, and the half-absorption bandwidth progressively widens. This occurs because the increase in neck radius reduces both the acoustic mass and acoustic resistance, leading to a decrease in the quality factor. Consequently, the resonant frequency increases, and the half-absorption bandwidth expands. Since the unit's impedance matches the air impedance across all neck radii, the peak absorption remains close to 1.

Figures 4(b)-(d) compare the distribution of the reflection coefficient on the complex plane for different neck radii. The reflection coefficient exhibits a pair of complex conjugate zeros and poles. When the loss and leakage are matched, the zeros lie precisely on the real axis, enabling the unit to perfectly absorb incident sound waves. Introducing loss can balance the radiation leakage, causing the zeros to shift toward the real axis. It can be observed that when the neck radius is 2.0 mm, the zero lies exactly on the real axis (indicated by the black dashed line). As the neck radius increases, the zero begins to move downward, gradually deviating from the real axis. This is due to the reduction in loss caused by the larger neck radius, transitioning the unit from a critically coupled state to an underdamped state. Additionally, the distance between the zero and pole represents the absorption bandwidth. It is evident that this distance increases with the neck radius, resulting in a progressively wider frequency bandwidth.

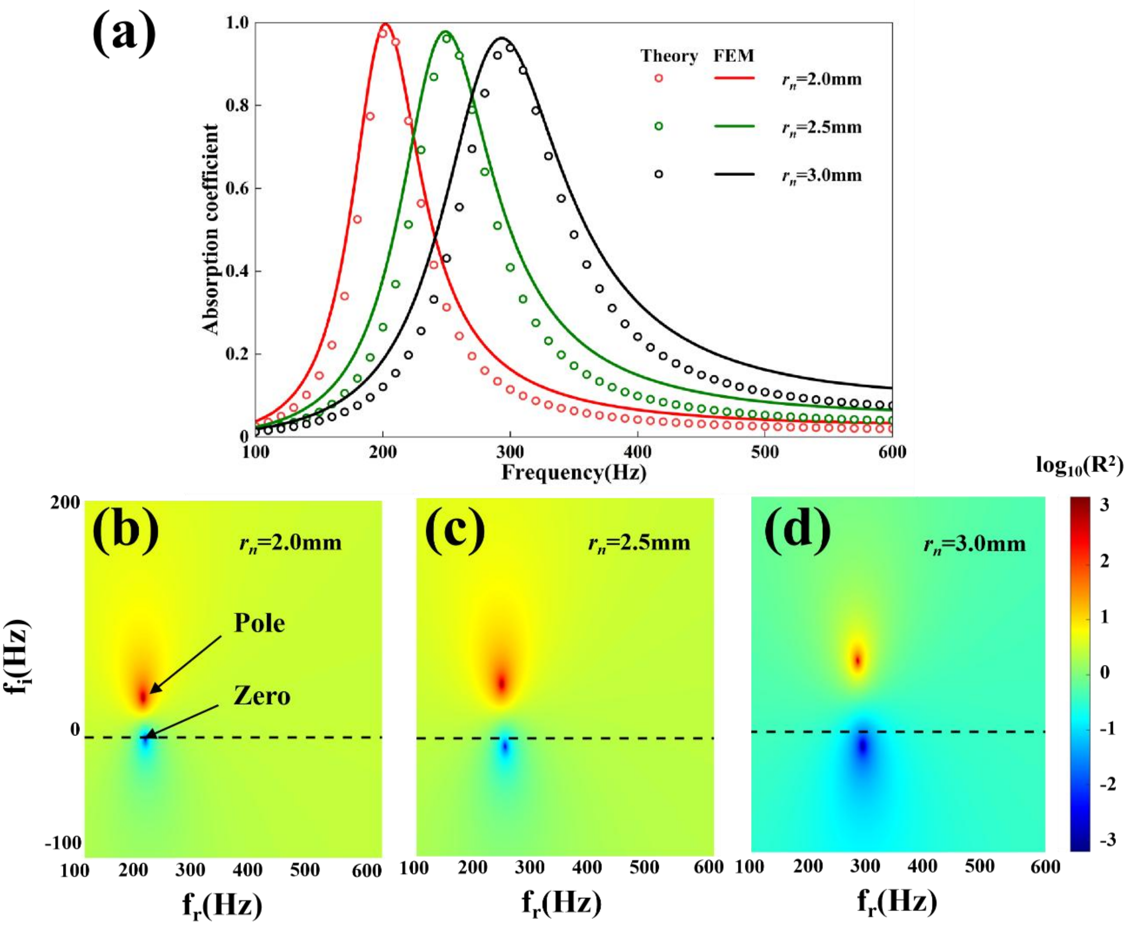

Figure 4. (a) Variation of sound absorption coefficient with neck radius r_n; (b)-(d) Distribution of reflection coefficient zeros and poles in the complex frequency plane for different neck radius

3.3. The Effect of Neck Length on Sound Absorption Performance

Figure 5(a) illustrates the sound absorption coefficients under different neck lengths ln, where the agreement between theoretical and numerical solutions validates the model's reliability. As the neck length decreases, the resonance absorption peak shifts toward higher frequencies, and its magnitude gradually diminishes. This occurs because a shorter neck reduces the effective mass of the air column inside the neck, thereby increasing the unit's resonance frequency. Simultaneously, shortening the neck decreases the viscous resistance encountered by the air moving within it, leading to a reduction in the neck's acoustic resistance. Consequently, the surface acoustic impedance of the unit deviates from the characteristic impedance of air, disrupting the impedance matching condition. As a result, more incident sound waves are reflected at the unit's surface, and less sound energy is effectively dissipated within the unit, leading to an overall decline in sound absorption performance.

Figures 5 (b)-(d) display the distribution of the reflection coefficient $log_{10}(R^2)$ on the complex plane for different neck lengths. It can be observed that when the neck length is 15 mm, the zero point is relatively distant from the real axis, indicating that the unit's damping struggles to achieve effective balance with the leakage of sound wave energy. As the neck length gradually increases, the thermo-viscous losses within the neck also rise, causing the zero point to move closer to the real axis. When the tube length reaches 35 mm, the zero point lies precisely on the real axis, achieving perfect sound absorption by the unit. Additionally, at tube lengths of 15 mm and 25 mm, the unit operates in an underdamped state, which broadens the absorption bandwidth by reducing the peak absorption magnitude.

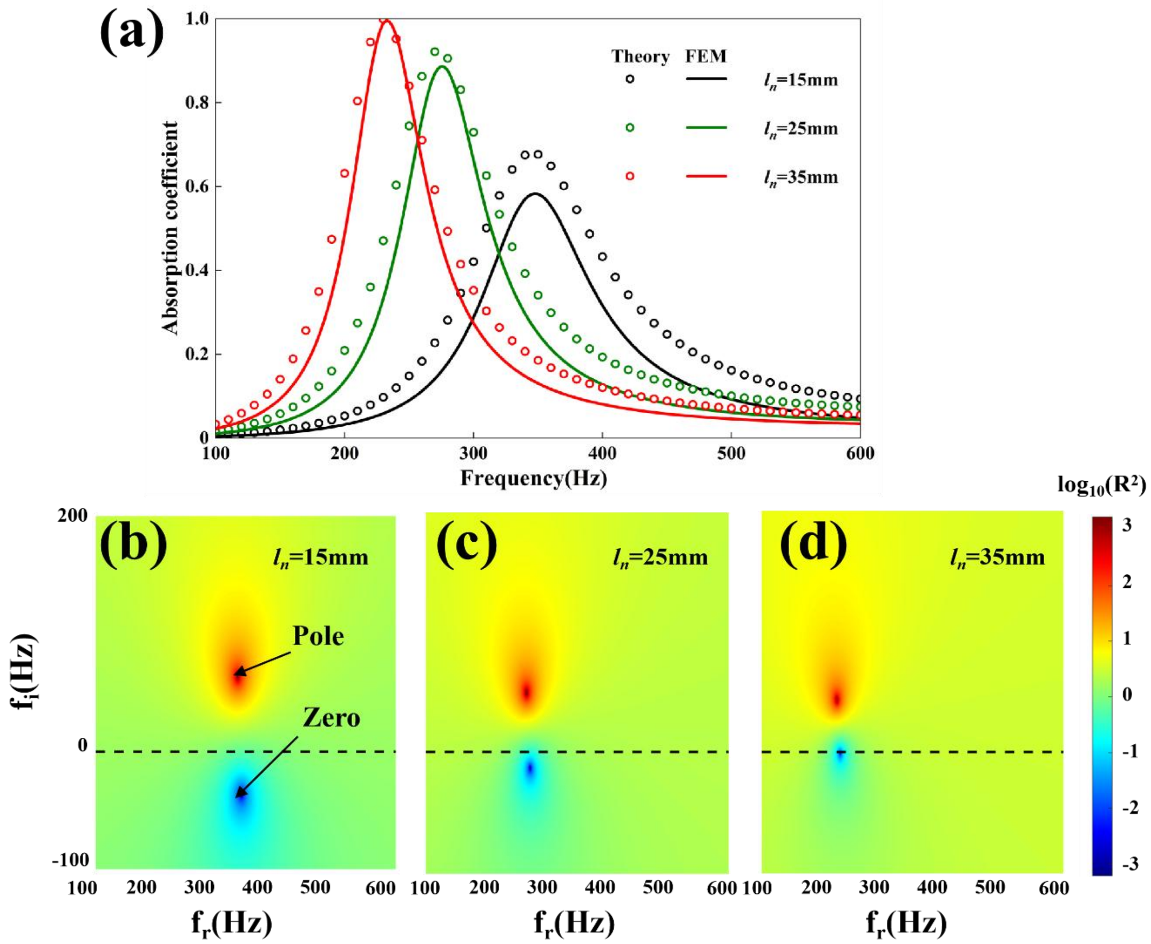

Figure 5. (a) Variation of sound absorption coefficient with neck length l_n; (b)-(d) Distribution of reflection coefficient zeros and poles in the complex frequency plane for different neck length

3.4. The Effect of Micro-Perforation Radius on Sound Absorption Performance

Figure 3-6(a) illustrates the sound absorption coefficients for different micro perforation radii r_p. As the micro perforation radius decreases, the resonance effect gradually weakens, the peak value declines, and the bandwidth significantly widens. There are two main reasons for these changes. First, the acoustic mass within the micro perforations increases as r_p decreases. Second, the reduction in r_p leads to an increase in the acoustic resistance of the micro perforations, causing the viscous resistance experienced by the air moving through the perforations to rise significantly. This results in the surface acoustic impedance deviating from the characteristic impedance of air, disrupting the impedance matching condition and creating an over-damped state, which weakens the energy dissipation capability and reduces the overall sound absorption coefficient.

Figures 3-6(b)-(d) show the distribution of the reflection coefficient log10(R2) on the complex plane for different micro perforation radii (r_p). It can be observed that when the micro perforation radius is 0.15 mm, the zero point is relatively far from the real axis, indicating that the damping of the unit has not effectively balanced the leakage of sound wave energy, placing the unit in an under-damped state. In this scenario, the absorption bandwidth is expanded by reducing the absorption peak. As the micro perforation radius gradually increases, the thermo-viscous losses within the perforations also rise, causing the zero point to move closer to the real axis. When the radius reaches 0.20 mm, the zero point almost lies on the real axis, achieving near-perfect sound absorption by the unit.

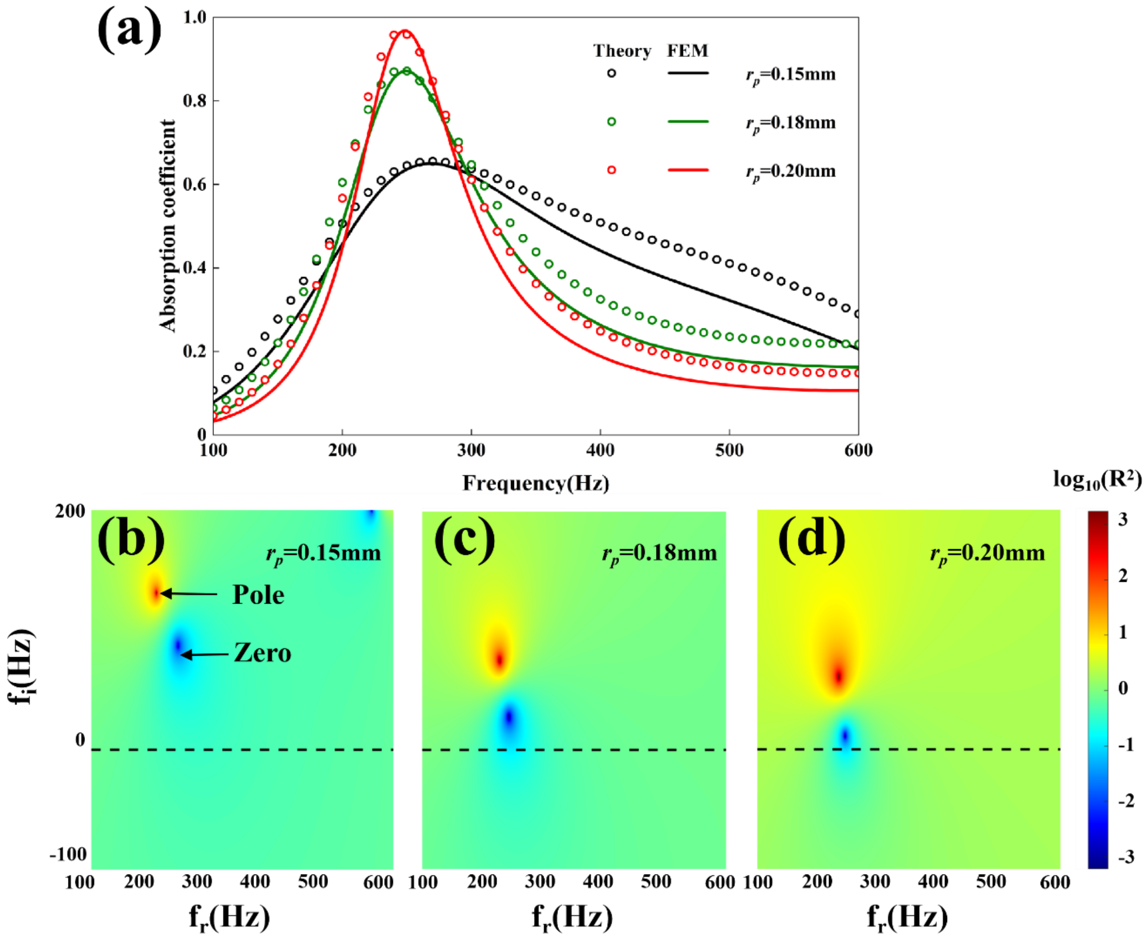

Figure 6. (a) Variation of sound absorption coefficient with micro-perforation radius r_p; (b)-(d) Distribution of reflection coefficient zeros and poles in the complex frequency plane for different micro-perforation radius

4. Design of Low-Frequency Broadband Sound-Absorbing Metamaterials

The above analysis indicates that the HREMPP unit can achieve efficient low-frequency sound absorption with a relatively thin physical thickness while maintaining its high-frequency sound absorption performance. However, the absorption bandwidth of a single unit is relatively limited in the low-frequency range. Numerous studies have shown that coupling multiple units with different parameters in parallel is an effective strategy for broadening the absorption bandwidth. Leveraging the highly tunable advantage of the HREMPP unit, two units with different peak absorption frequencies can be coupled in parallel under the constraint of maintaining an overall thickness of 50 mm, thereby achieving a broader absorption bandwidth. Only the neck radius rn of the units was varied: the neck radius of unit 1 was set to r_{n1}=2 mm, and that of unit 2 to r_{n2}=3 mm. The remaining dimensional parameters were designed as follows: a=25 mm, t=1 mm, l_n=30 mm, n_p=30, r_p=0.25 mm, t_{fp}=2 mm, and d_p=3 mm. For ease of expression, the two units are referred to as HREMPP1 and HREMPP2, respectively.

As shown in Figure 6(a), HREMPP1 and HREMPP2 exhibit two distinct near-perfect absorption peaks at 208 Hz and 284 Hz, respectively. The half-absorption bandwidth ranges from 176 Hz to 358 Hz. The peak frequencies are largely consistent with those of each individual unit, though slight shifts occur due to coupling effects near the adjacent unit entrances. However, the peak absorption of each unit does not decrease, and the absorption bandwidth is somewhat broadened.

In the complex frequency plane plot of Figure 6(b), the zeros corresponding to the absorption peaks lie on or near the real axis, indicating near-perfect sound absorption. Figure 6(c) displays the real and imaginary parts of the designed acoustic metamaterial's effective impedance. The real part of the effective impedance equals the characteristic impedance of ambient air, while the imaginary part becomes zero at the two frequencies of 210 Hz and 281 Hz. Within the 200–300 Hz range, the impedance spectrum shows a certain degree of elevation. This rise between absorption peaks is caused by anti-resonances between different types of HREMPP units. Nevertheless, due to the substantial dissipation in the necks and micro perforations, these anti-resonances do not lead to a significant drop in the absorption spectrum. The designed acoustic metamaterial still exhibits a wider and flatter absorption coefficient compared to individual units, demonstrating its excellent tunable sound absorption performance.

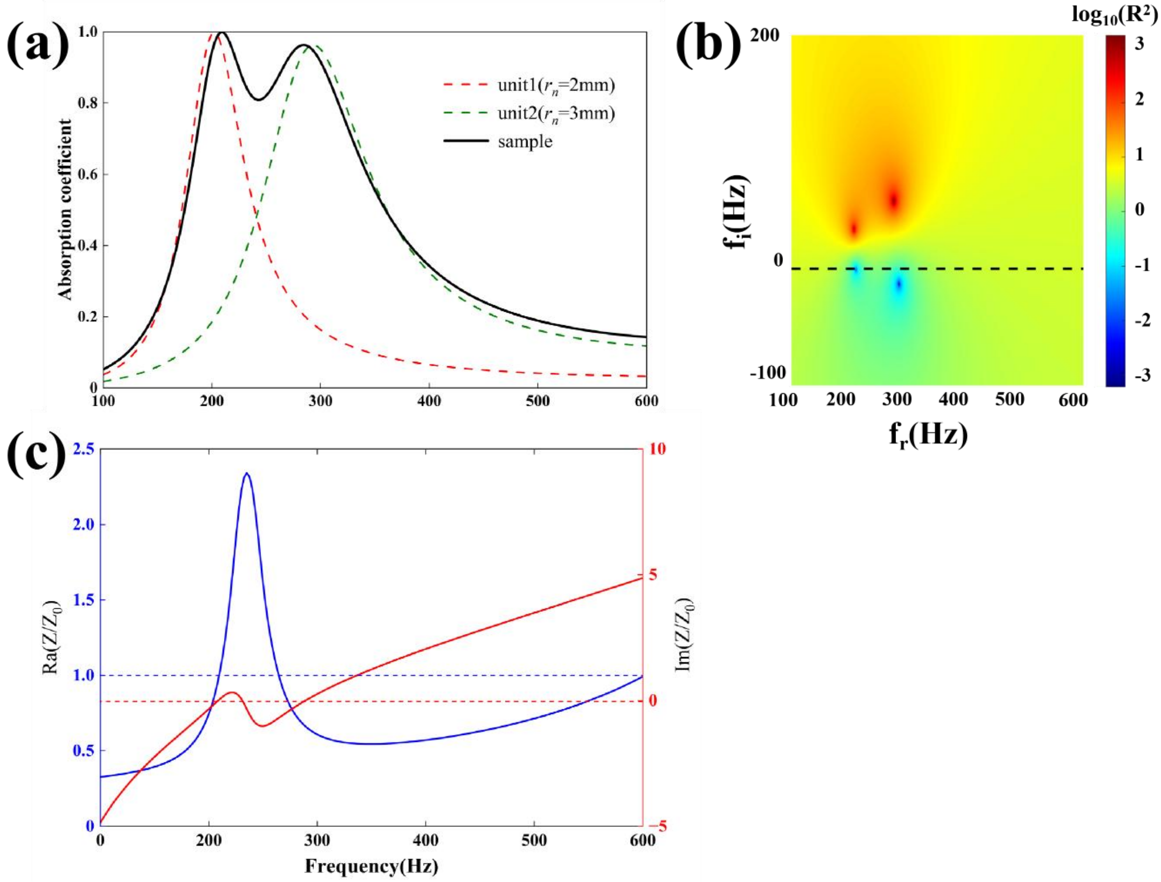

Figure 7. (a) Sound-absorbing metamaterials and the sound absorption coefficient curve of each constituent unit; (b) Distribution of reflection coefficient zeros and poles in the complex frequency plane for sound-absorbing metamaterials; (c)Sound impedance curve of sound-absorbing metamaterials

5. Summary

This study designs and investigates a novel low-frequency sound-absorbing metamaterial featuring an embedded micro-perforated panel Helmholtz resonator (HREMPP). By integrating a micro-perforated panel (MPP) parallel to the cavity of a conventional Helmholtz resonator (HR), an innovative HREMPP unit structure is created. A comprehensive theoretical model was established using the electro-acoustic analogy method, demonstrating excellent agreement with finite element simulation results. Analysis reveals that the HREMPP unit achieves near-perfect absorption at 250 Hz with a subwavelength thickness of only 50 mm, exhibiting a half-absorption bandwidth (210-300 Hz) 50% wider than traditional HRs, primarily attributed to enhanced viscous and thermal dissipation mechanisms introduced by the MPP.

Through in-depth analysis in the complex frequency plane, the influence of three key parameters on sound absorption performance was examined: increasing the neck radius broadens the bandwidth but raises the resonance frequency; shortening the neck length elevates the frequency while reducing peak absorption; decreasing the micro-perforation radius lowers the peak but widens the bandwidth. Finally, leveraging the easily tunable resonance frequency of HREMPP units, two units with different neck radii (2 mm and 3 mm respectively) were coupled in parallel while maintaining a total thickness of 50 mm, successfully constructing a low-frequency broadband sound-absorbing metamaterial. This coupled structure generates two near-perfect absorption peaks at 208 Hz and 284 Hz, forming an efficient wideband absorption range from 176 Hz to 358 Hz, effectively addressing the narrow bandwidth limitation of single units and providing a viable solution for designing ultra-thin, broadband low-noise control devices.

References

[1] Cai X, Guo Q, Hu G, et al. Ultrathin low-frequency sound absorbing panels based on coplanar spiral tubes or coplanar Helmholtz resonators [J]. Applied Physics Letters, 2014, 105(12): 121901.

[2] Liu L, Chang H, Zhang C, et al. Single-channel labyrinthine metasurfaces as perfect sound absorbers with tunable bandwidth [J]. Applied Physics Letters, 2017, 111(8): 083503.

[3] Shen Y, Yang Y, Guo X, et al. Low-frequency anechoic metasurface based on coiled channel of gradient cross-section [J]. Applied Physics Letters, 2019, 114(8): 083501

[4] Huang S, Fang X, Wang X, et al. Acoustic perfect absorbers via Helmholtz resonators with embedded apertures [J]. The Journal of the Acoustical Society of America, 2019, 145(1): 254-262.

[5] Ryoo H, Jeon W. Dual-frequency sound-absorbing metasurface based on visco-thermal effects with frequency dependence [J]. Journal of Applied Physics, 2018, 123(11): 115110.

[6] Wu X, Fu C, Li X, et al. Low-frequency tunable acoustic absorber based on split tube resonators [J]. Applied Physics Letters, 2016, 109(4): 043501.

[7] Zhang J, Zeng Q, Hou H, Xiao Y, Cheng B, Xia Z. Study of the noise reduction performance of acoustic enclosures with ultra-thin bending labyrinth metasurfaces. Appl Acoust 2025; 231:110447.

[8] Duan M, Yu C, Xin F, Lu TJ. Tunable underwater acoustic metamaterials via quasiHelmholtz resonance: from low-frequency to ultra-broadband. Appl Phys Lett 2021; 118(7):071904.

[9] Zhang C, Hu X. Three-dimensional single-port labyrinthine acoustic metamaterial: Perfect absorption with large bandwidth and tunability [J]. Physical Review Applied, 2016, 6(6): 064025.

[10] Yang M, Chen S, Fu C, et al. Optimal sound-absorbing structures [J]. Materials Horizons, 2017, 4(4): 673-680.

[11] Z. Xiao, P. Gao, D. Wang, X. He, Y. Qu, L. Wu, Accelerated design of low frequency broadband sound absorber with deep learning approach, Mech. Syst. Signal Process. 211 (2024) 111228, http://dx.doi.org/10.1016/j.ymssp.2024. 111228.